International Journal of Solids and Structures 47 (2010) 2841–2854

Contents lists available at ScienceDirect

International Journal of Solids and Structures

journal homepage: www.elsevier.com/locate/ijsolstr

Modeling elasto-plastic indentation on layered materials using the equivalent inclusion method

W. Wayne Chen, Kun Zhou, Leon M. Keer, Q. Jane Wang *

Department of Mechanical Engineering, Northwestern University, Evanston, IL 60208, USA

ARTICLE INFO

Article history:
Received 28 September 2009
Received in revised form 29 May 2010
Available online 17 June 2010

Keywords:
Elasto-plastic
Layer
Contact
Equivalent inclusion method

ABSTRACT

This paper develops a fast semi-analytical model for solving the three-dimensional elasto-plastic contact problems involving layered materials using the Equivalent Inclusion Method (EIM). The analytical elastic solutions of a half-space subjected to a unit surface pressure and a unit subsurface eigenstrain are employed in this model; the topmost layer is simulated by an equivalent inclusion with fictitious eigenstrain. Accumulative plastic deformation is determined by a procedure involving an iterative plasticity loop and an incremental loading process. Algorithms of the fast Fourier transform (FFT) and the Conjugate Gradient Method (CGM) are utilized to improve the computation efficiency. An analytical elastic solution of layered body contact (O'Sullivan and King, 1988) and an indentation experiment result involving a layered substrate (Michler et al., 1999) are used to examine the accuracy of this model. Comparisons between numerical results from the present model and a commercial FEM software (Abaqus) are also presented. Case studies of a rigid ball loaded against a layered elasto-plastic half-space are conducted to explore the effects of the modulus, yield strength, and thickness of the coating on the hardness, stiffness, and plastic deformation of the composite body.

1. Introduction

Coatings are widely used for surface reinforcement, friction and wear reduction, and fatigue prevention (Bhushan and Peng, 2002; Tichy and Meyer, 2000). Protective coating layers can be found in many engineering applications including cutting tools, cams, gears, magnetic storage media, and biomedical devices, some of which may involve plastic deformation under a heavy-duty condition. In the presence of material dissimilarity between the layer and the substrate, the contact stresses may differ remarkably from those developed in a homogeneous body. A numerical elasto-plastic contact model for layered bodies is thus necessary to assist coating material choice and layer design.

The elastic layered contact is an analytically complicated problem. The spatial dimensions of the governing differential equations of elasticity are generally reduced by using the integral transform methods, such as the Hankel (Burmister, 1945) and Fourier transforms (Chen, 1971; Ju and Chen, 1984; Plumet and Dubourg, 1998). The displacements and stresses in a layered body can be solved in a hybrid space-frequency domain. O'Sullivan and King (1988) extended the method given by Chen (1971) to compute the subsurface stress field in a layered half-space subjected to distributed surface pressure and shear tractions; and Nogi and Kato (1997) developed the explicit frequency response functions of elastic field for a purely pressure-loaded layered body. The O'Sullivan and King approach has been extensively used by many researchers (Liu and Wang, 2002; Liu et al., 2005, 2007; Polonsky and Keer, 2000, 2001).

Numerical methods are generally required to solve the problem of the elasto-plastic contact between layered solids. A good review on the numerical methods applied to the layered contact problems was given by Bhushan and Peng (2002). Peng and Bhushan (2001, 2002) developed a layered body contact model for elastic/plastic solids with computer-generated rough surfaces using a variational principle method. The elastic-perfectly plastic behavior of a material is approximately simulated by using a cut off value (i.e., the hardness of the softer material) to limit the contact pressure. This approximate technique may give an efficient evaluation of the real contact area and the gap between contacting rough surfaces, however, it also leads to incorrect subsurface stress and strain fields because the residual stress and plastic deformation are not considered. The finite element method (FEM) has been extensively used by many researchers to perform the numerical studies of elasto-plastic indentation problems involving homogeneous (Hardy et al., 1971; Follansbeea and Sinclairb, 1984; Mesarovic and Fleck, 1999) and layered (Komvopoulos, 1989; Tian and Saka, 1991; Kral and Komvopoulos, 1996; Kral and Komvopoulos, 1997; Ye and Komvopoulos, 2003) materials. The FEM is flexible enough to solve the problems with complicated geometries and

* Corresponding author. Tel.: +1 (847) 467 7510.
E-mail address: qwang@northwestern.edu (Q.J. Wang).

0020-7683/$ - see front matter © 2010 Elsevier Ltd. All rights reserved.
doi:10.1016/j.ijsolstr.2010.06.011

Nomenclature

Letters

a_0	Hertz contact radius based on material properties of substrate, mm
A_c	contact area, mm^2
A_{ijkl}	influence coefficient of stress by eigenstrain or plastic strain
B^n_{ij}, B^t_{ij}	influence coefficients of stresses by pressure and shear traction
C^c_{ijkl}, C^s_{ijkl}	elastic moduli of layer and substrate, GPa
D^p, D^t, D^{es}	influence coefficients of displacements by pressure, shear, and eigenstrain
E_b, E_c, E_s	Young's moduli of mating body, coating, and substrate, GPa
E^*	equivalent Young's moduli, GPa
G^p, G^t	the Green's functions of displacement by pressure and shear traction
h, h_i	surface gap, initial surface clearance, mm
N_1, N_2, N_3	element numbers along three axes
N_c	number of element in the coating along the z-axis
p	contact pressure, MPa
p_0	Hertz peak pressure based on material properties of substrate, MPa
R	radius of indenter, μm
s	shear traction, MPa
S_{ij}	the deviatoric stress, MPa
t	coating thickness, mm
T^n_{ij}, T^t_{ij}	the Green's functions of stresses caused by contact pressure and shear traction
u_3	surface normal displacement, mm
$u_3^{(1)}$, $u_3^{(2)}$	normal displacements caused by pressure and eigenstrain, mm
W	normal indentation load, N
W_c	transitional load leading to the onset of plasticity, N
x, y, z	space coordinates, mm

Greek letters

μ_e	equivalent shear moduli, GPa
μ_f	friction coefficient
δ	rigid body approach, mm
$2\Delta_1$, $2\Delta_2$, $2\Delta_3$	element sizes along three axes, mm
ε_{ij}, ε^p_{ij}, ε^*_{ij}	total material distortion, plastic strain, and equivalent eigenstrain
λ	effective plastic strain
ν_b, ν_c, ν_s	Poisson ratios of mating body, coating, and substrate
σ_{ij}, σ_{VM}	total stress and the von Mises stress, MPa
σ_{Yc}, σ_{Ys}	yield strengths of coating and substrate, MPa
$\sigma^{(1)}_{ij}$, $\sigma^{(2)}_{ij}$, $\sigma^{(3)}_{ij}$	stresses caused by pressure, plastic strain, eigenstrain, MPa
Ω_c, Ω_s, Ψ_p	domains of coating, substrate, and plastically deformed material

material constitutive responses. However, a large number of elements is needed to mesh the entire layered body, which may increase the computation burden significantly.

A three-dimensional semi-analytical method (SAM) developed by Jacq et al. (2002) to study the elasto-plastic contacts is based on the exact solutions of uniform eigenstrains in a single cubic inclusion in a half-space derived by Chiu (1978). This approach has been further used to study the elasto-plastic contact problems involving friction, wear, thermal loading, and rough surfaces (Antaluca and Nelias, 2008; Boucly et al., 2005, 2007; Chen and Wang, 2008; Chen et al., 2008a,b; Nelias et al., 2006, 2007a,b; Wang and Keer, 2005). Chiu (1980) also derived two-dimensional analytical solutions for a layer on a rigid frictionless half-plane with eigenstrains.

The purpose of this paper is to develop a fast semi-analytical model for three-dimensional elasto-plastic contact of layered bodies. The simulation domain is discretized into small cuboidal elements, and the approach of calculating eigenstresses in a half-space proposed by Jacq et al. (2002) is used. The Equivalent Inclusion Method (EIM) previously developed for the inhomogeneous inclusion problem (Mura, 1982) is utilized here to simulate the stress disturbance due to the layer effect. Using the Conjugate Gradient Method (CGM) (Polonsky and Keer, 1999) and the discrete convolution and fast Fourier transform (DC-FFT) algorithm (Liu et al., 2000) will yield high computation efficiency, which makes the solutions of problems requiring fine mesh or transient analysis feasible. The simulations can provide detailed information of the surface pressure, subsurface stress, and plastic deformation.

2. Theoretical background

2.1. Contact problem description and modeling

Consider the contact of a ball (E_b, ν_b) with a layered half-space, where the elastic constants of coating and substrate materials are (E_c, ν_c) and (E_s, ν_s), respectively. The origin of the Cartesian coordinate system is set to be the initial contact point, and the z-axis points inwards the layered half-space (Fig. 1). The increasing normal load W pushes the sphere into the layered half-space, and both the coating and substrate materials may yield when the stress exceeds their elastic limits. The resulting plastic strains are denoted by ε^p_{ij}. The surfaces of two bodies are assumed to be smooth. It should be noted that a similar numerical procedure has been used to solve the elasto-plastic contact of homogeneous bodies with rough surfaces (Chen et al., 2007). Hence, this model can be readily extended to treat rough surfaces without increasing the numerical complexity.

In order to simplify the problem, the sphere is treated as an elastic homogeneous body. The coating is assumed to be perfectly bonded to the substrate without interface slipping and locally detaching. Surface adhesion is not considered in this model (i.e.,

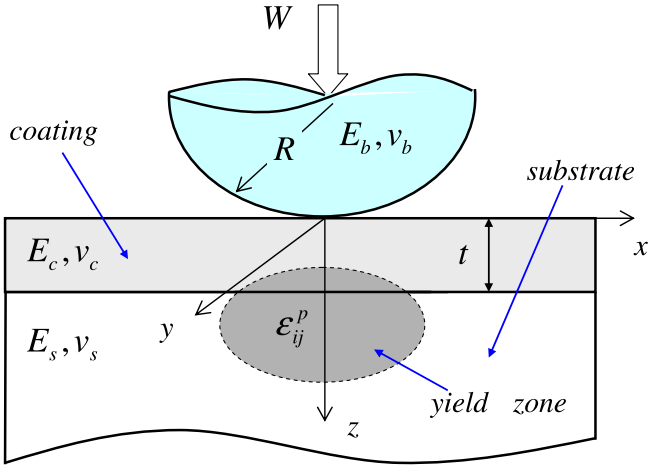

Fig. 1. Elasto-plastic contact of a sphere with a layered substrate.

the normal tensile traction is not allowed at the interface). A dry contact is governed by the following equations:

$$W = \int_{-\infty}^{\infty}\int_{-\infty}^{\infty} p(x,y)\cdot dx\,dy \tag{1}$$

$$h(x,y) = h_i(x,y) + u_3(x,y) - \delta \tag{2}$$

where p is the contact pressure, u_3 the normal displacement of contact bodies, h_i the initial surface geometry (h_i approximately equals $(x^2+y^2)/2R$ when the sphere radius R is much larger than the contact area dimensions), and h and δ are the surface gap and the rigid body approach, respectively. The interfacial interaction results in a contact area A_c, where pressures are positive and the surface gap vanishes:

$$p(x,y) > 0, \quad h(x,y) = 0, \quad (x,y) \in A_c \tag{3}$$

In the non-contact area,

$$p(x,y) = 0, \quad h(x,y) > 0, \quad (x,y) \notin A_c \tag{4}$$

2.2. Equivalent inclusion method for layered medium

The presence of the coating layer disturbs the contact deformation, stress field, and further plasticity. The domains of layer, substrate, and the plasticity can be denoted by Ω_c, Ω_s, and Ψ_p, respectively (Fig. 2). The elastic moduli of layer and substrate materials, C^c_{ijkl} and C^s_{ijkl}, are given as

$$C^m_{ijkl} = \lambda_m\delta_{ij}\delta_{kl} + \mu_m(\delta_{ik}\delta_{jl} + \delta_{il}\delta_{jk}) \quad (m = c \text{ or } s) \tag{5}$$

where λ_m and μ_m are the Lamé's constants with $\lambda_m = E_m\nu_m/(1+\nu_m)(1-2\nu_m)$ and $\mu_m = E_m/2(1+\nu_m)$, and δ_{ij} is the Kronecker delta function. In light of the Hooke's law, the stresses in Ω_c can be expressed as

$$\sigma_{ij} = C^c_{ijkl}(\varepsilon_{kl} - \varepsilon^p_{kl}) \quad \text{in } \Omega_c \tag{6}$$

Here, ε_{kl} is the total strain caused by the external contact loading, and simply equals the elastic strain in a plasticity-free domain (i.e., $\varepsilon^p_{kl} = 0$ in $\Omega_c \cap \overline{\Psi}_p$).

Eigenstrain is a term referring the inelastic strain, such as thermal strain, plastic strain, and misfit strain, while eigenstress is the stress disturbance caused by the eigenstrain distribution. The EIM was used to study the disturbance of the stress field in an infinitely extended matrix containing an inhomogeneous inclusion, which has material constants different from those of the surrounding matrix and may have its own eigenstrains (Mura, 1982). With this method, the layer is replaced by a homogenous inclusion that occupies the coating space Ω_c and has a fictitious (equivalent) eigenstrain ε^*_{ij}. Thus, the stress disturbance due to the material inhomogeneity of the layer is modeled by the eigenstress due to eigenstrain inside the virtual inclusion. The elastic strains in the inclusion can then be written as $\varepsilon_{kl} - \varepsilon^p_{kl} - \varepsilon^*_{kl}$. Because the Hooke's law still holds, the stresses in the inclusion are

$$\sigma_{ij} = C^s_{ijkl}(\varepsilon_{kl} - \varepsilon^p_{kl} - \varepsilon^*_{kl}) \quad \text{in } \Omega_c \tag{7}$$

The necessary and sufficient conditions for the equivalence of the stresses in the above two problems of layered body and inclusion are given as (Fig. 2)

$$\sigma_{ij} = C^c_{ijkl}(\varepsilon_{kl} - \varepsilon^p_{kl}) = C^s_{ijkl}(\varepsilon_{kl} - \varepsilon^p_{kl} - \varepsilon^*_{kl}) \quad \text{in } \Omega_c \tag{8}$$

Elimination of $(\varepsilon_{kl} - \varepsilon^p_{kl})$ in Eq. (8) leads to the following relationship between the equivalent eigenstrains and total stresses:

$$C^s_{ijkl}C^{c^{-1}}_{klab}\sigma_{ab} - \sigma_{ij} = C^s_{ijkl}\varepsilon^*_{kl} \quad \text{in } \Omega_c \tag{9}$$

where $C^{c^{-1}}_{ijkl} = -\delta_{ij}\delta_{kl}\nu_c/E_c + (\delta_{ik}\delta_{jl} + \delta_{il}\delta_{jk})/4\mu_c$ is the elastic compliance of the coating material; subscripts (i,j,k,l,a,b) range over 1, 2, 3, and the index summation convention holds. As shown in Section 2.3, the subsurface eigenstresses can be obtained as a function of equivalent eigenstrains ε^*_{ij} when the eigenstrains are in a homogeneous material. Thus, Eq. (9) is an implicit equation with respect to unknown ε^*_{ij}. A numerical iteration method is used to determine ε^*_{ij}, which will be discussed in Section 2.6.

A fast Fourier transform (FFT) based contact algorithm is used to improve the computational efficiency in this model. Application of FFT extends the data series (stress, strain, or displacement) periodically to form an infinite series, which may cause an alias (periodic) error for a non-periodic problem (e.g., a point contact with localized contact area). Liu et al. (2000) proposed an efficient method with zero-padding and wrap-around order techniques to avoid this periodic error (only the contributions from the excitations in the target domain are taken in account). However, the issue brought by this method is that the fictitious inclusion outside the target domain can not be captured. Thus, the actual problem solved by this model (based on the approach of Liu et al. (2000)) is that of a block embedded in the substrate, where the block is of the same material as the layer and the horizontal dimensions of block are the same as those of the simulation domain. Neglecting the coating outside the simulation domain will cause unexpected error on the stress field especially at the domain boundary. However, a sufficiently large simulation domain (about 8 times the contact radius based on the following validation cases) can make this error negligible because the layer structure outside the domain has trivial influence on the elastic field near the load application region. For a periodic

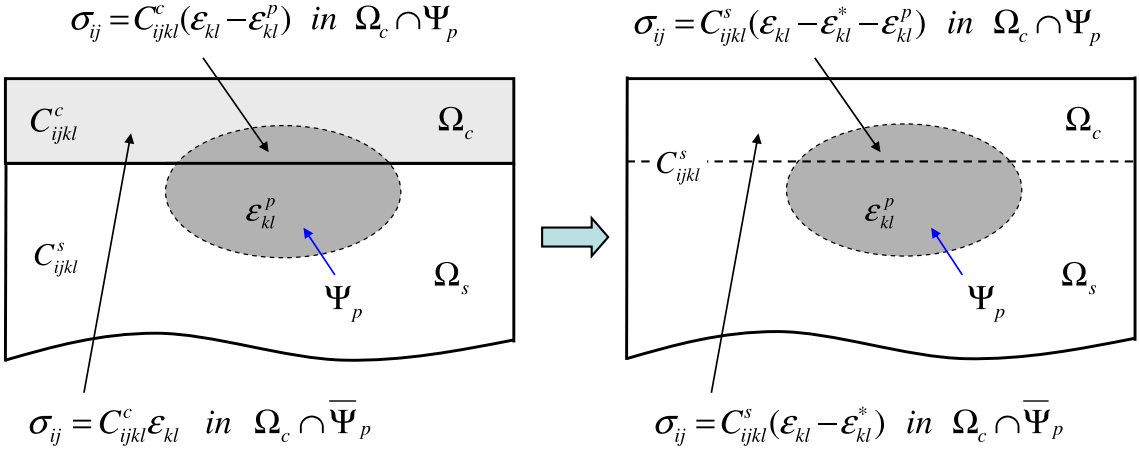

Fig. 2. Equivalent inclusion method to solve the coating-induced stress disturbance (Ω_c, Ω_s, Ψ_p, $\overline{\Psi}_p$ are the domains of coating, substrate, plastically deformed material, and elastically deformed material, respectively).

problem (e.g., nominally flat-on-flat surface contact), the periodic boundary condition of this kind of problem naturally fulfills the requirement of periodic extension of the FFT algorithm. Thus, the periodic error can be completely circumvented.

2.3. Calculation of subsurface stress

Subsurface stress calculation is a necessary step towards the understanding of plastic deformation evolution. In a layered elasto-plastic contact body, subsurface stresses are composed of three parts: (1) the contact stress due to surface pressure p and shear traction s, (2) the residual stress due to plastic strain ε^p_{ij}, and (3) the disturbance stress due to equivalent eigenstrain ε^*_{ij}. The stresses caused by ε^p_{ij} and ε^*_{ij} are essentially eigenstresses.

Elastic contact stresses $\sigma^{(1)}_{ij}$ at (x,y,z) in a homogeneous half-space of the substrate material caused by arbitrarily distributed surface pressure $p(x',y')$ and shear traction $s(x',y')$ along the x-axis can be calculated using the followed two dimensional integrals:

$$\sigma^{(1)}_{ij}(x,y,z) = \int_{-\infty}^{\infty}\int_{-\infty}^{\infty}\left[T^n_{ij}(x-x',y-y',z) + \mu_f \cdot T^t_{ij}(x-x',y-y',z)\right] \cdot p(x',y')dx'\,dy' \tag{10}$$

Here, Coulomb friction $s(x',y') = \mu_f \cdot p(x',y')$ is assumed in Eq. (10) with a friction coefficient μ_f. T^n_{ij} and T^t_{ij} are the Green's functions of the stresses due to the unit concentrated normal and tangential forces at the surface origin (Johnson, 1985), which are listed in Appendix.

The domain of interest is meshed using small cubic elements of the same size $2\Delta_1 \times 2\Delta_2 \times 2\Delta_3$. N_1, N_2, and N_3 are the element numbers along the x, y, and z directions, respectively. Pressure in each discrete surface patch is treated as constant and given by the value at the face center of patch. $p_{[\alpha,\beta]}$ is the pressure of the element centered at $(2\alpha\Delta_1, 2\beta\Delta_2)$. Stresses and strains in each subsurface cubic element are also treated to be constant; $\sigma^{(1)}_{ij_{[\alpha,\beta,\gamma]}}$ denote the elastic stresses at point $(2\alpha\Delta_1, 2\beta\Delta_2, 2\gamma\Delta_3)$, which are chosen to represent the stresses of the element centered at this point. The elastic contact stresses at the discrete elements can be written as

$$\sigma^{(1)}_{ij[\alpha,\beta,\gamma]} = \sum_{\xi=0}^{N_1-1}\sum_{\psi=0}^{N_2-1}\left(B^n_{ij[\alpha-\xi,\beta-\psi,\gamma]} + \mu_f \cdot B^t_{ij[\alpha-\xi,\beta-\psi,\gamma]}\right)p_{[\xi,\psi]} \quad (0 \leqslant \alpha \leqslant N_1-1,\ 0 \leqslant \beta \leqslant N_2-1)$$

where

$$B^J_{ij[\alpha-\xi,\beta-\psi,\gamma]} = \int_{(2\xi-1)\Delta_1}^{(2\xi+1)\Delta_1}\int_{(2\psi-1)\Delta_2}^{(2\psi+1)\Delta_2} T^J_{ij}(2\alpha\Delta_1 - x', 2\beta\Delta_2 - y', 2\gamma\Delta_3)dx'\,dy' \quad (J = n \text{ and } t). \tag{11}$$

In Eq. (11), the indefinite double integrals of T^n_{ij} and T^t_{ij} (also see Appendix) used to calculate the influence coefficients $B^n_{ij[\alpha-\xi,\beta-\psi,\gamma]}$ and $B^t_{ij[\alpha-\xi,\beta-\psi,\gamma]}$ were derived by Love (1929).

Jacq et al. (2002) developed an approach of calculating the residual stresses due to plastic strain based on the original work of Chiu (1978), who derived eigenstress solutions of a single cuboidal inclusion with uniform eigenstrains in a homogeneous semi-infinite body. The approach of Jacq et al. (2002) is used here to determine eigenstresses caused by plastic strain ($\sigma^{(2)}_{ij}$) and equivalent eigenstrain ($\sigma^{(3)}_{ij}$). Eigenstresses of the element centered at $(2\alpha\Delta_1, 2\beta\Delta_2, 2\gamma\Delta_3)$ can be expressed as

$$\begin{aligned}\sigma^{(2)}_{ij[\alpha,\beta,\gamma]} &= \sum_{\xi=0}^{N_1-1}\sum_{\psi=0}^{N_2-1}\sum_{\varphi=0}^{N_3-1} A_{ijkl[\alpha-\xi,\beta-\psi,\varphi,\gamma]}\varepsilon^p_{kl[\xi,\psi,\varphi]}\\ \sigma^{(3)}_{ij[\alpha,\beta,\gamma]} &= \sum_{\xi=0}^{N_1-1}\sum_{\psi=0}^{N_2-1}\sum_{\zeta=0}^{Nc-1} A_{ijkl[\alpha-\xi,\beta-\psi,\zeta,\gamma]}\varepsilon^*_{kl[\xi,\psi,\zeta]}\end{aligned} \tag{12}$$

$(0 \leqslant \alpha \leqslant N_1-1,\ 0 \leqslant \beta \leqslant N_2-1,\ 0 \leqslant \gamma \leqslant N_3-1)$

where $A_{ijkl[\alpha-\xi,\beta-\psi,\zeta,\gamma]}$ are the influence coefficients, whose detailed formulas are given by Jacq et al. (2002), and N_c is the number of elements in the coating domain Ω_c along the z direction.

Assume that the deformation is small and within the limit of linear elasticity theory. Superposition principle is still applicable here. The total stresses can be expressed as the summation of the contact stresses and eigenstresses:

$$\sigma_{ij[\alpha,\beta,\gamma]} = \sigma^{(1)}_{ij[\alpha,\beta,\gamma]} + \sigma^{(2)}_{ij[\alpha,\beta,\gamma]} + \sigma^{(3)}_{ij[\alpha,\beta,\gamma]} \tag{13}$$

2.4. Calculation of surface normal displacement

The surface normal displacement can be decomposed as follows: (1) the elastic displacement due to surface normal pressure, and (2) the eigen-displacement due to subsurface eigenstrains. The elastic normal displacement at (x,y) on a homogeneous half-space can be associated with distributed pressure $p(x',y')$ and shear traction $s(x',y') = \mu_f \cdot p(x',y')$ along the x-axis using the Boussinesq integral:

$$u^{(1)}_3(x,y) = \int_{-\infty}^{\infty}\int_{-\infty}^{\infty}\left[G^p(x-x',y-y') + \mu_f \cdot G^t(x-x',y-y')\right] \cdot p(x',y')dx'\,dy'$$

where $G^p(x,y) = \frac{1}{\pi E^*\sqrt{x^2+y^2}}$, $G^t(x,y) = \frac{x}{\pi\mu_e(x^2+y^2)}$,

$$\frac{1}{E^*} = \frac{(1-\nu_s^2)}{E_s} + \frac{(1-\nu_b^2)}{E_b} \quad \text{and} \quad \frac{1}{\mu_e} = \frac{(1+\nu_s)(1-2\nu_s)}{2E_s} - \frac{(1+\nu_b)(1-2\nu_b)}{2E_b} \tag{14}$$

Here, G^p and G^s are the Green's functions, and E^* and μ_e are the equivalent Young's modulus and shear modulus. The surface of interest is discretized into $N_1 \times N_2$ rectangular elements, each of which has a size of $2\Delta_1 \times 2\Delta_2$. Pressure and displacement in each discrete patch are treated as constant and given by the values at the center of patch. $p_{[\alpha,\beta]}$, $s_{[\alpha,\beta]}$, and $u^{(1)}_{3[\alpha,\beta]}$ denote pressure, shear traction, and elastic displacement of the element centered at $(2\alpha\Delta_1, 2\beta\Delta_2)$, respectively. The discrete formula of elastic displacement becomes

$$u^{(1)}_{3[\alpha,\beta]} = \sum_{\xi=0}^{N_1-1}\sum_{\psi=0}^{N_2-1}\left(D^p_{[\alpha-\xi,\beta-\psi]} + \mu_f \cdot D^t_{[\alpha-\xi,\beta-\psi]}\right)p_{[\xi,\psi]} \quad (0 \leqslant \alpha \leqslant N_1-1,\ 0 \leqslant \beta \leqslant N_2-1)$$

where

$$D^J_{[\alpha-\xi,\beta-\psi]} = \int_{(2\xi-1)\Delta_1}^{(2\xi+1)\Delta_1}\int_{(2\psi-1)\Delta_2}^{(2\psi+1)\Delta_2} G^J(2\alpha\Delta_1 - x', 2\beta\Delta_2 - y')dx'\,dy' \quad (J = n \text{ and } t) \tag{15}$$

Here, $D^p_{[\alpha-\xi,\beta-\psi]}$ and $D^t_{[\alpha-\xi,\beta-\psi]}$ are the influence coefficients, and the closed-form indefinite integrals of the Green's functions G^p and G^t are given as

$$\begin{aligned}\iint G^p(x,y)dx\,dy &= \frac{1}{\pi E^*}\left[x\ln\left(y+\sqrt{x^2+y^2}\right) + y\ln\left(x+\sqrt{x^2+y^2}\right)\right]\\ \iint G^t(x,y)dx\,dy &= \frac{1}{\pi\mu_e}\left[y\ln\left(\sqrt{x^2+y^2}\right) + x\tan^{-1}(y/x)\right]\end{aligned} \tag{16}$$

Two sources cause the surface eigen-displacement: plastic strain ε^p_{ij} and equivalent eigenstrain ε^*_{ij}. Jacq et al. (2002) derived the exact solution of normal displacement using the reciprocal theorem specifically for the volume-conserved plastic strain. Following the procedure of Jacq et al. (2002), the normal eigen-

displacement of a homogeneous half-space at the surface point (x,y) caused by a general eigenstrain can be expressed as a volume integral:

$$u_3^{(2)}(x,y) = \frac{1}{P}\int_{-\infty}^{\infty}\int_{-\infty}^{\infty}\int_{-\infty}^{\infty}\varepsilon_{ij}^{**}(x',y',z')\sigma_{ij}^{n}(x'-x,y'-y,z')dx'\,dy'\,dz' \tag{17}$$

Here, $\varepsilon_{ij}^{**} = \varepsilon_{ij}^{*} + \varepsilon_{ij}^{p}$ are the total eigenstrains (plastic plus equivalent). $\sigma_{ij}^{n}(x'-x,y'-y,z')$ are the elastic stresses at (x',y',z') caused by the concentrated normal force P at the surface point (x,y). Note that there are nine component products in the integrand due to the summation convention. Consider the same cubic element system used in Section 2.3. $\varepsilon_{ij[\alpha,\beta,\gamma]}^{**}$ denote the eigenstrains at the point of $(2\alpha\Delta_1, 2\beta\Delta_2, 2\gamma\Delta_3)$, which are chosen to represent the uniform eigenstrains of the cubic element centered at this point. $u_{3[\alpha,\beta]}^{(2)}$ denotes the normal eigen-displacement at $(2\alpha\Delta_1, 2\beta\Delta_2)$. Thus, Eq. (17) can be discretized as

$$u_{3[\alpha,\beta]}^{(2)} = \sum_{\xi=0}^{N_1-1}\sum_{\psi=0}^{N_2-1}\sum_{\zeta=0}^{N_3-1} D_{ij[\xi-\alpha,\psi-\beta,\zeta]}^{es}\varepsilon_{ij[\xi,\psi,\zeta]}^{**} \quad (0 \leqslant \alpha \leqslant N_1-1,\ 0 \leqslant \beta \leqslant N_2-1)$$

where

$$D_{ij[\xi-\alpha,\psi-\beta,\zeta]}^{es} = \int_{(2\xi-1)\Delta_1}^{(2\xi+1)\Delta_1}\int_{(2\psi-1)\Delta_2}^{(2\psi+1)\Delta_2}\int_{(2\zeta-1)\Delta_3}^{(2\zeta+1)\Delta_3} T_{ij}^{n}(x'-2\alpha\Delta_1, y'-2\beta\Delta_2, z')dx'\,dy'\,dz' \tag{18}$$

Here, $D_{ij[\xi-\alpha,\psi-\beta,\zeta]}^{es}$ are the influence coefficients, and the indefinite triple integrals of T_{ij}^{n} are given in Appendix. Note that the equation $\sigma_{ij}^{n} = P\cdot T_{ij}^{n}$ is used in deriving Eq. (18) from Eq. (17).

Finally, the total normal displacement is the eigen-displacement plus the elastic one:

$$u_{3[\alpha,\beta]} = u_{3[\alpha,\beta]}^{(1)} + u_{3[\alpha,\beta]}^{(2)} \tag{19}$$

2.5. Plasticity consideration

In this study, both the layer and substrate materials are assume to behave as elastic-perfectly plastic bodies without strain hardening. σ_{Yc} and σ_{Ys} denote yield strengths of coating and substrate, respectively. The J-2 criterion for material yield initiation (valid for most metal materials) is given as

$$\begin{aligned} f &= \sigma_{VM} - \sigma_{Yc} \quad \text{in } \Omega_c \\ f &= \sigma_{VM} - \sigma_{Ys} \quad \text{in } \Omega_s \end{aligned} \tag{20}$$

Here, $\sigma_{VM} = \sqrt{3S_{ij}:S_{ij}/2}$ is the von Mises equivalent stress, and $S_{ij} = \sigma_{ij} - \sigma_{kk}\delta_{ij}/3$ the deviatoric stress. Yielding occurs when the von Mises equivalent stress exceeds the material yield strength. The elastic-perfectly plasticity model well represents the plastic responses of many engineering metallic materials under simple loading scenarios, such as normal indentation. If the reverse plasticity due to unloading and plastic accumulation due to repeated contacts are of interest, a more realistic strain hardening law needs to be used. The semi-analytical models (SAM) of elasto-plastic contact have been developed to analyze contacts of materials with different hardening behaviors, including the linear, power, isotropic, and kinetic laws (Jacq et al., 2002; Wang and Keer, 2005; Chen et al., 2008b). Sharing the same numerical framework for the plasticity loop with SAM, the present coating indentation model is capable of handling different hardening law of plasticity.

2.6. Numerical procedure

Plasticity is nonlinear and depends on the loading history. Therefore, an incremental loading process has to be simulated to capture the plastic strain accumulation. The entire loading process is divided into N_L quasi-static steps, and each step has a constant load. Each load step starts from the normal contact problem, where the half-space is assumed to be homogeneous and plasticity-free. From Eqs. (2) and (15), the contact equation can be written as

$$0 = h_{i[\alpha,\beta]} - \delta + \sum_{\xi=0}^{N_1-1}\sum_{\psi=0}^{N_2-1}\left(D_{[\alpha-\xi,\beta-\psi]}^{p} + \mu_f D_{[\alpha-\xi,\beta-\psi]}^{t}\right)p_{[\xi,\psi]} \quad \text{in } A_c \tag{21}$$

This linear equation system with an unknown pressure distribution can be solved by the single-loop CGM (Polonsky and Keer, 1999). The DC-FFT algorithm proposed by Liu et al. (2000) is also introduced to enhance the computational efficiency.

Once the contact pressure is obtained from the contact solution, the subsurface contact stress field can be evaluated by Eq. (11). The J-2 criterion is used to identify the trial plastic domain where the von Mises stress exceeds the local yield strength. The actual increment of the effective plastic strain $d\lambda$ is the value that returns the J-2 yield function to zero, i.e., $f(\lambda + d\lambda) = 0$; $\lambda = \sum d\lambda = \sum\left(\sqrt{2d\varepsilon_{ij}^{p}d\varepsilon_{ij}^{p}/3}\right)$ is the effective accumulative plastic strain. Here, the Newton–Raphson method is used to solve $d\lambda$ (Chen et al., 2008b). Increments of the plastic strain tensor $d\varepsilon_{ij}^{p}$ can then be calculated by the general flow rule:

$$d\varepsilon_{ij}^{p} = d\lambda\frac{3S_{ij}}{2\sigma_{VM}} \tag{22}$$

Next, the equivalent eigenstrains ε_{ij}^{*} caused by the material inhomogeneity are determined using the EIM. Substitution of Eq. (13) into Eq. (9) yields

$$\begin{aligned} &\mathbf{L}:\left(\boldsymbol{\sigma}_{[\alpha,\beta,\gamma]}^{(1)} + \boldsymbol{\sigma}_{[\alpha,\beta,\gamma]}^{(2)} + \boldsymbol{\sigma}_{[\alpha,\beta,\gamma]}^{(3)}\right) = \boldsymbol{\varepsilon}_{[\alpha,\beta,\gamma]}^{*} \quad \text{in } \Omega_c \\ &\mathbf{L} = \mathbf{C}^{c^{-1}} - \mathbf{C}^{s^{-1}} \end{aligned} \tag{23}$$

Here, the tensor form is used to simplify the formula; $\mathbf{C}^s$, $\mathbf{C}^c$, and $\mathbf{L}$ are the fourth order tensors of material constant, and $\boldsymbol{\sigma}$ and $\boldsymbol{\varepsilon}$ are the second order tensors. Considering the expressions of eigenstresses in Eq. (12), we have

$$\begin{aligned} \boldsymbol{\varepsilon}_{[\alpha,\beta,\gamma]}^{*} - \mathbf{L}:\sum_{\xi=0}^{N_1-1}\sum_{\psi=0}^{N_2-1}\sum_{\zeta=0}^{Nc-1}\mathbf{A}_{[\alpha-\xi,\beta-\psi,\zeta,\gamma]}:\boldsymbol{\varepsilon}_{[\xi,\psi,\zeta]}^{*} &= \mathbf{L}:\boldsymbol{\sigma}_{[\alpha,\beta,\gamma]}^{(1)} + \mathbf{L}:\sum_{\xi=0}^{N_1-1}\sum_{\psi=0}^{N_2-1}\sum_{\varphi=0}^{N_3-1}\mathbf{A}_{[\alpha-\xi,\beta-\psi,\varphi,\gamma]}:\boldsymbol{\varepsilon}_{[\xi,\psi,\varphi]}^{p} \\ &(0 \leqslant \alpha,\ \xi \leqslant N_1-1,\ 0 \leqslant \beta, \\ &\psi \leqslant N_2-1,\ 0 \leqslant \varphi \leqslant N_3-1,\ 0 \leqslant \gamma,\ \zeta \leqslant N_c) \end{aligned} \tag{24}$$

where $\mathbf{A}$ is the fourth order tensor of the influence coefficient. Eq. (24) is a linear system with $6N_1N_2N_c$ equations and $6N_1N_2N_c$ unknown eigenstrains $\varepsilon_{ij[\alpha,\beta,\gamma]}^{*}$ in elements within the coating domain. An iterative numerical approach based on the conjugate gradient algorithm is applied to obtain equivalent eigenstrains (Zhou et al., under review). Solving the eigenstresses in a half-space can be accelerated by a three-dimensional FFT method proposed by Zhou et al. (2009).

Inserting the plastic strain and the equivalent eigenstrain into Eq. (18), one can calculate the surface normal eigen-displacement. The eigen-displacement in turn alters the surface contact geometry and the contact pressure distribution. Therefore, the interfacial contact has to be solved again to update the contact pressure. A closed-loop linking the variations of the contact pressure, plastic strain, and surface geometry is developed. This loop is repeated

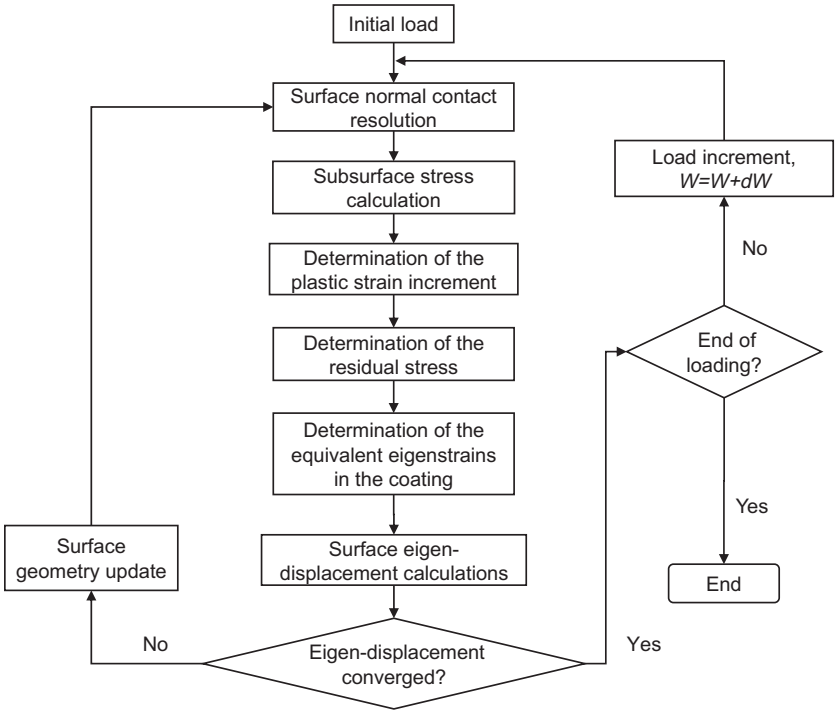

Fig. 3. Flowchart of the numerical procedure.

until the difference between the eigen-displacements of two adjacent iterative steps is less than the prescribed error tolerance. Once the convergence reaches, the normal load is increased and the next load step begins. The flowchart of the entire numerical procedure is shown in Fig. 3.

3. Results of elastic indentation of a layered substrate

The elastic solution of contact pressure between a spherical indenter and a layered half-space was developed by O'Sullivan and King (1988) in terms of a series of basic functions, which was also utilized to calculate the subsurface stress field in the layer and substrate based on the explicit frequency response functions. In order to verify the accuracy of the present model, the numerical results of the present model are compared with those from the O' Sullivan and King's solutions (see Fig. 4). Here, a_0 and p_0 are Hertz solutions of the contact radius and peak pressure, which are obtained for a homogenous half-space of the substrate material. The coating thickness, t, is taken to be a_0, and Poisson ratios of layer and substrate are 0.3. The simulation domain of $(8a_0 \times 8a_0 \times 2.5a_0)$ is meshed into $128 \times 128 \times 40$ cubic elements. Fig. 4(a) shows pressure profiles beneath the indenter for the cases with different E_c/E_s. The increase in the coating modulus increases the contact pressure and reduces the contact area. Stress profiles of σ_{11} along the depth at the origin are given in Fig. 4(b). In the case of a stiffer coating, σ_{11} becomes tensile at the coating-substrate interface. Fig. 4(c) gives the interfacial shear stress σ_{13} along x-axis. Excellent agreements can be found between the present numerical results and the solutions given by O'Sullivan and King (1988). Another noteworthy point is that shear stress σ_{13} at the boundary of simulation domain predicted by the present model matches well with that given by O'Sullivan and King (1988). It indicates that the domain sizes used in this study are large enough to avoid the boundary error induced by neglecting the layer structure outside the simulation domain.

In order to demonstrate the mesh size effect, different mesh densities are used to compute the elastic indentation of a substrate with a stiffer coating, and the results of von Mises stress σ_{VM} along the depth inside the coating are presented in Fig. 5. Increasing the mesh density may improve the quality of simulation results (smoothly capture the stress variation) and decrease the numerical error. The fine mesh $128 \times 128 \times 40$ yields a stress profile closely matching with the analytical solution given by O'Sullivan and King (1988), and it is sufficiently accurate for the numerical studies performed in this paper.

Fig. 6 shows the simulation results of the stiffer coating case ($E_c/E_s = 2$) when the Coulomb friction is taken into account. Contact pressure distributions beneath the indenter and von Mises stress σ_{VM} profiles along the depth are given in Fig. 6(a) and (b), respectively. A strong interaction between pressure and shear traction is indicated in Fig. 6(a). Increase in the shear traction can elevate the peak contact pressure and shift its position towards the trailing edge of the contact area. With increasing friction coefficient, a significant rise in the von Mises stress inside the coating is identified as well. However, the effect of shear traction on von Mises stress in the substrate is trivial. In this case, the shear traction is assumed to be linearly proportional to the local pressure. However, the real distribution of shear traction can be determined through solving the tangential contact equation, in which the surface tangential displacements due to eigenstrain and contact stresses are of primary interest.

4. Results of elasto-plastic indentation of a layered substrate

4.1. Model validation

Michler et al. (1999) measured the load–displacement curve for an indentation experiment of a 10 μm-radius diamond indenter on a tooling steel substrate coated with a 3.5 μm diamond-like carbon (DLC) layer, where only the steel substrate involves obvious plastic deformation (the DLC layer has a relatively high hardness of about 25 GPa (Michler et al., 1999) and can be considered to be purely elastic in the mechanical model). The present model is applied to simulate this experiment for the purpose of model validation.

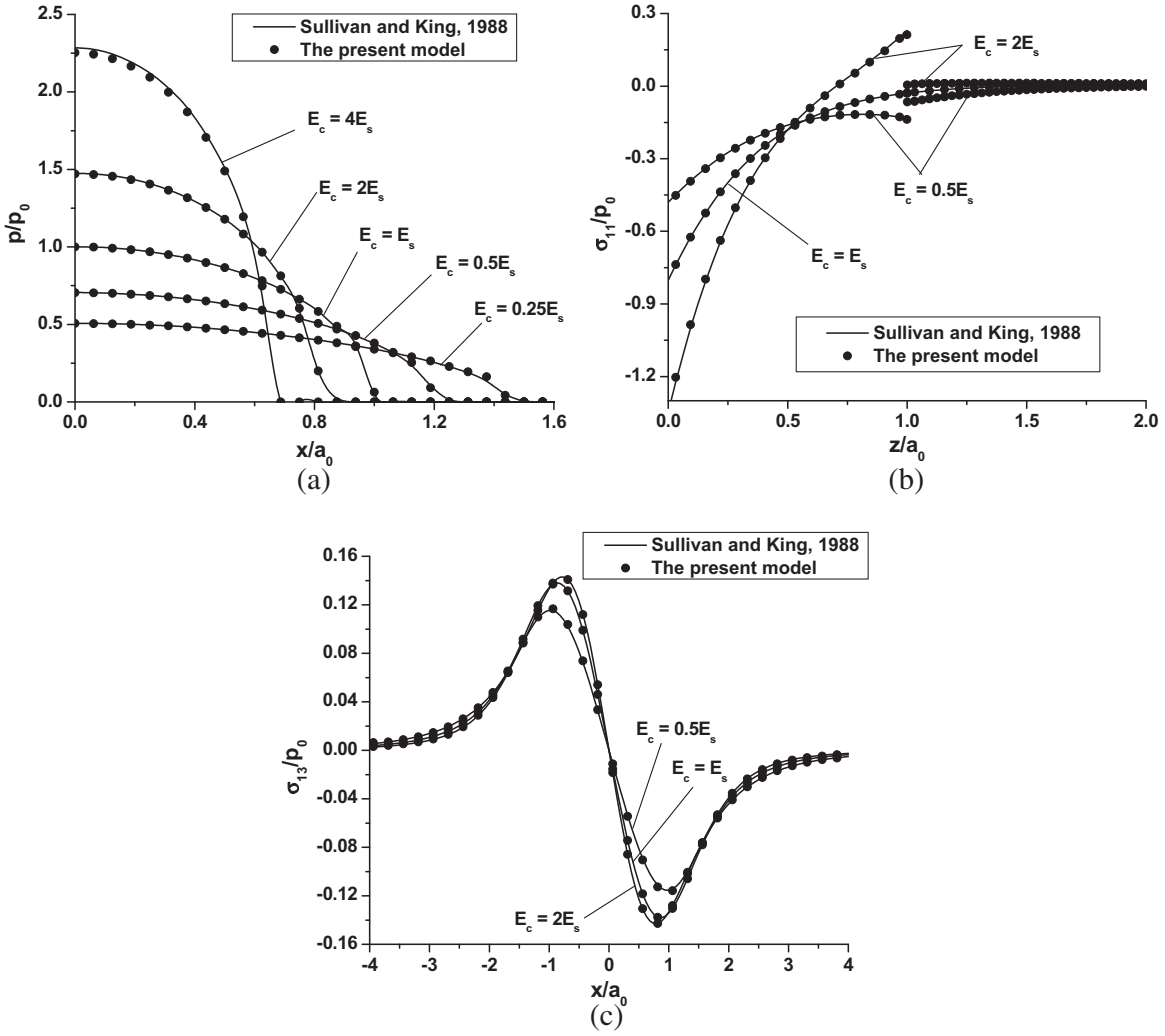

Fig. 4. Model validation with the O'Sullivan and King's solutions: (a) contact pressure along the x-axis, (b) σ_{11} along the depth at the origin, and (c) σ_{13} along the x-axis at the coating-substrate interface.

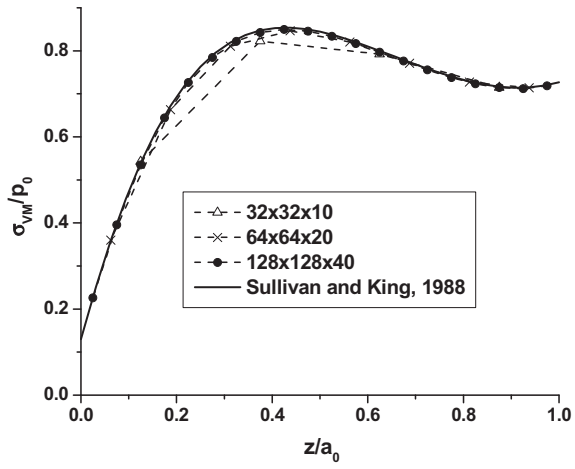

Fig. 5. Profiles of von Mises stress σ_{VM} in coating along the depth obtained from different mesh densities (the stiffer coating case $E_c/E_s = 2$).

The elastic constants of the DLC layer ($E_c = 87$ GPa and $\nu_c = 0.22$) reported by Cho et al. (1999) were used. All material properties used in the simulation are listed in Fig. 7 for clarity. The load–displacement curves from the experiment (Michler et al., 1999) and the present model are plotted in Fig. 7. The numerical result from the present model well matches the experiment measurement. It should be noted that the indentation behaviors may be altered by the presence of pre-existing strains, which may occur during the coating or surface finishing processes. Extensive experimental and numerical studies have been conducted to explore the relationship between the load–displacement response of nano-indentation and the pre-existing stress field (Bolshakov et al., 1996; Suresh and Giannakopoulos, 1998; Carlsson and Larsson, 2001; Giannakopoulos, 2003). Although the results shown in Fig. 7 did not include the effect of such residual strains, pre-existing strains can be taken into account in the present model as initial eigenstrains, which can be readily incorporated into ε^p_{kl} in Eqs. (6)–(9).

4.2. Parametric study: Young's modulus of the layer

In the following parametric studies, coating's thickness t is comparable with or less than the contact radius; and both the layer and the substrate have elastic-perfectly plastic behaviors subjected to plastic strain accumulation. Poisson ratios of them are 0.3. The sphere is assumed to be rigid. Young's modulus and yield strength of the substrate are fixed at $E_s = 200$ GPa and $\sigma_{Ys} = 350$ MPa. The maximum normal load is $W/W_c = 30$, where W_c is the transitional load indicating the onset of an elasto-plastic contact if the ball is

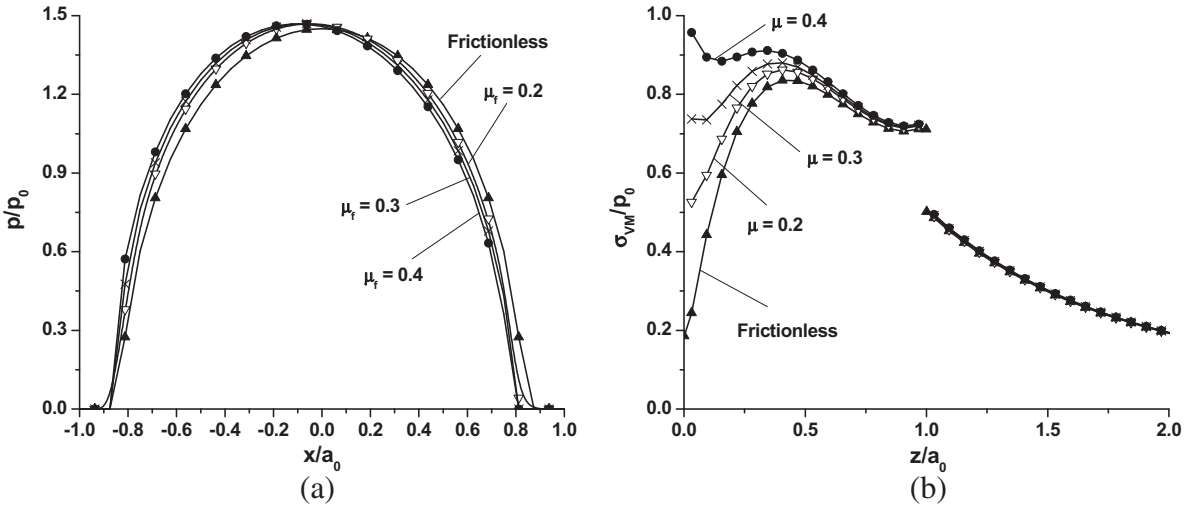

Fig. 6. Effects of surface shear traction on the simulation results (the stiffer coating case $E_c/E_s = 2$|): (a) contact pressure along the x-axis, and (b) von Mises stress σ_{VM} along the depth at the contact center.

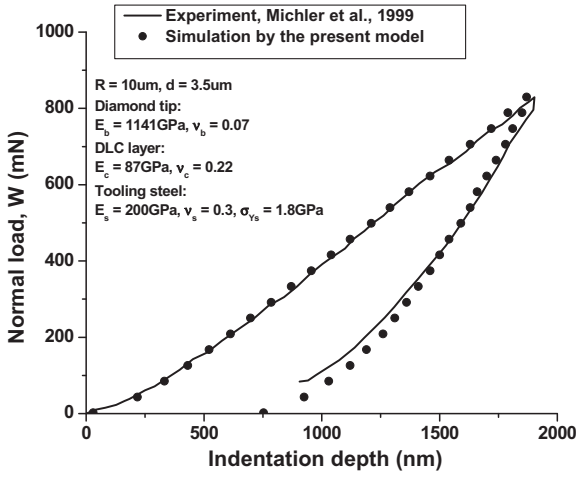

Fig. 7. Model validation with the experiment measurement by Michler et al. (1999); the load–displacement curves for an indentation of an $R = 10$ μm diamond spherical tip into a DLC coated tooling steel involving only substrate plasticity (because the DLC coating has a relatively high hardness of about 25 GPa (Michler et al., 1999)).

loaded against the homogeneous half-space of the substrate material (Johnson, 1985). The value of W_c is given by

$$W_c = \frac{(1.6\pi\sigma_{Ys})^3}{6}\left(\frac{R}{E^*}\right)^2 \tag{25}$$

Here, R is the sphere radius. In the following results, the displacements are normalized by a_0, the stresses and pressure by p_0, and the normal loads by W_c. a_0 and p_0 are Hertz solutions of contact radius and peak pressure when the indenter is loaded against the substrate without coating and the normal load is $20W_c$. The simulation domain sizes and the mesh number are the same as those used in the cases in Section 3. Each simulation case includes 20 loading steps as well as 20 unloading steps. 'Hard' and 'soft' are used to describe the magnitude of yield strength (hardness), and 'stiff' and 'compliant' the magnitude of Young's modulus.

A set of simulations are first conducted for the cases with fixed substrate Young's modulus and varied layer modulus, and simulation results are presented in Figs. 8–11. Here, the ratio between yield strengths of the layer and the substrate is $\sigma_{Yc}/\sigma_{Ys} = 1.5$, and the coating thickness is $t = 0.5a_0$. For the purpose of model comparison, the commercial finite element (FE) software, Abaqus, was also utilized to simulate the same indentation problems on the layered materials. The deformed half-space is meshed using Abaqus C3D4 elements, whose sizes are exactly the same to those used by the present model in the potential contact region. Both numerical models were run on a computer with 2.4 GHz CPU and 2G memory. It took about 2 hours for the present model to complete the simulation of one case, while about 14 hours for the Abaqus FE model. Evolutions of contact pressure from both the present model and FEM are presented in Fig. 8 with respect to increasing normal load. An appreciably good agreement is found between the pressure profiles obtained from the two methods, which also serves as a proof to the accuracy of the present model.

Under a lighter load ($W/W_c = 3$), the pressure profiles resemble the Hertz solutions, and the central peak pressure in the stiffer coating case ($E_c/E_s = 2$) is larger than that in the more compliant coating case ($E_c/E_s = 0.5$). Under a heavier load ($W/W_c = 30$), the pressure has a relatively flat profile in the compliant coating case while the pressure has a concave shape with a reduced value at the contact center and a uplifted value at the edge in the stiffer coating case. Similar conclusions were also reported in the previous research works (Kennedy and Ling, 1974; Komvopoulos, 1989; Kral and Komvopoulos, 1996). The overall load bearing capacity is not improved obviously through the usage of a stiffer coating. The numerical test predicts that the dimensionless contact areas $A_c/\pi a_0^2$ are 2.001, 1.841, and 1.682 for the cases of $E_c/E_s = 0.5$, 1, and 2, respectively.

The boundaries of plastic regions in the plane of $y = 0$ developed at different normal loads for the cases of $E_c/E_s = 0.5$ and 2 are plotted in Fig. 9. Only one half of the plane is shown due to symmetry. In the contact body with a more compliant layer, the plastic deformation initiates just below the coating-substrate interface and then propagates to the coating, while in the body with a stiffer coating, the plastic deformation initiates in the coating under a smaller indentation load. Increase in the layer modulus expands the size of plastic region in the coating. The contact pressure and subsurface stresses are enhanced by a stiffer coating if only a purely elastic contact is considered. However, the maximum stress in an elasto-plastic layer is limited by the layer yield strength, which is fixed in these cases; thus more material needs to deform plastically to accommodate the external load. In the case with a stiffer coating, the plastic region expands and reaches the surface, which may cause unexpected plasticity wear; more plastically deformed material under the surface makes the surface contact more

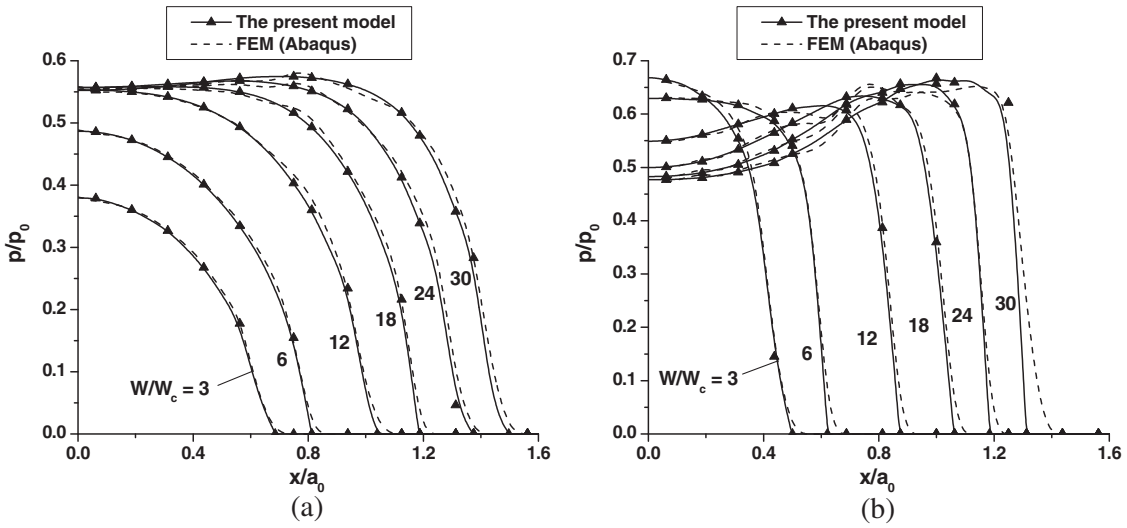

Fig. 8. Contact pressure profiles along the x-axis with the increasing normal load (results from the present model and FEM): (a) the more compliant coating case ($E_c/E_s = 0.5$), and (b) the stiffer coating case ($E_c/E_s = 2$).

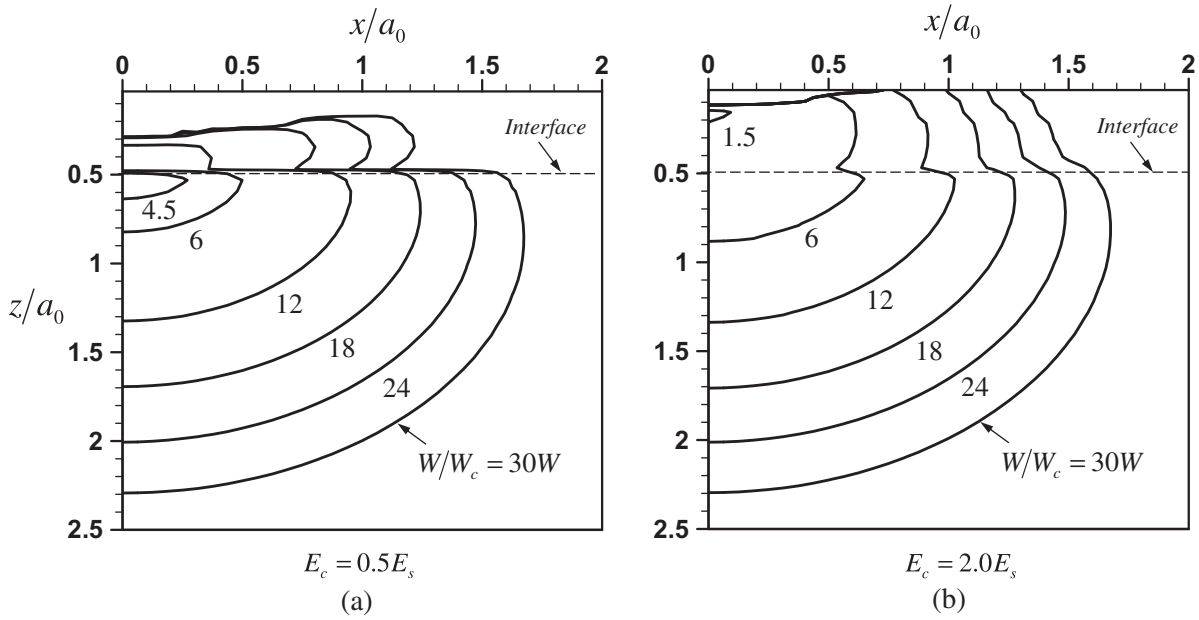

Fig. 9. Evolutions of the plastic region with the increasing normal load: (a) the more compliant coating case ($E_c/E_s = 0.5$), and (b) the stiffer coating case ($E_c/E_s = 2$).

conformal, which may explain why the pressure in the stiffer coating case drops in the center of contact area and the overall load bearing capacity is barely improved (see Fig. 8(b)). The sizes of plastic regions in the substrate under $W = 30W_c$ for the two cases with different layer moduli are almost the same.

The von Mises stress contours under the maximum indentation load ($W = 30W_c$) for the more compliant and stiffer coating cases are given in Fig. 10(a) and (b), respectively. Here, the von Mises stress is normalized by the yield strength of substrate, σ_{Ys}. In the elastic solutions of the layered body contact problems discussed by O'Sullivan and King (1988), the maximum von Mises stress developed in a more compliant layer is lower than that in a stiffer layer. However, in the elasto-plastic solutions predicted by the present model, it is found that the maximum von Mises stresses in the layer are the same for the two cases because the von Mises stress in the layer are bounded by the layer yield strength (fixed in the two cases). This is consistent with the elastic-perfectly plastic material property used in these simulations. Similarly, the maximum von Mises stresses in the substrate are found to be the same in the two cases as well. Fig. 11 presents the load–displacement curves for three cases with the varied layer modulus, where the slopes of loading and unloading curves from a stiffer coating case are larger than those from a more compliant coating case; the body with a stiffer coating has a shallower indentation depth at the end of loading. However, the depths of the residual impressions are almost the same for these three cases. It is shown that increasing modulus of the layer reinforces the stiffness of a layered body but hardly improves its hardness (or strength).

4.3. Parametric study: yield strength of the layer

Fig. 12 shows the comparisons of simulation results from five cases with varied yield strength of the layer, i.e., $\sigma_{Yc}/\sigma_{Ys} = 0.75$, 1, 1.5, 2, and 4. Here, the Young's moduli of the layer and substrate

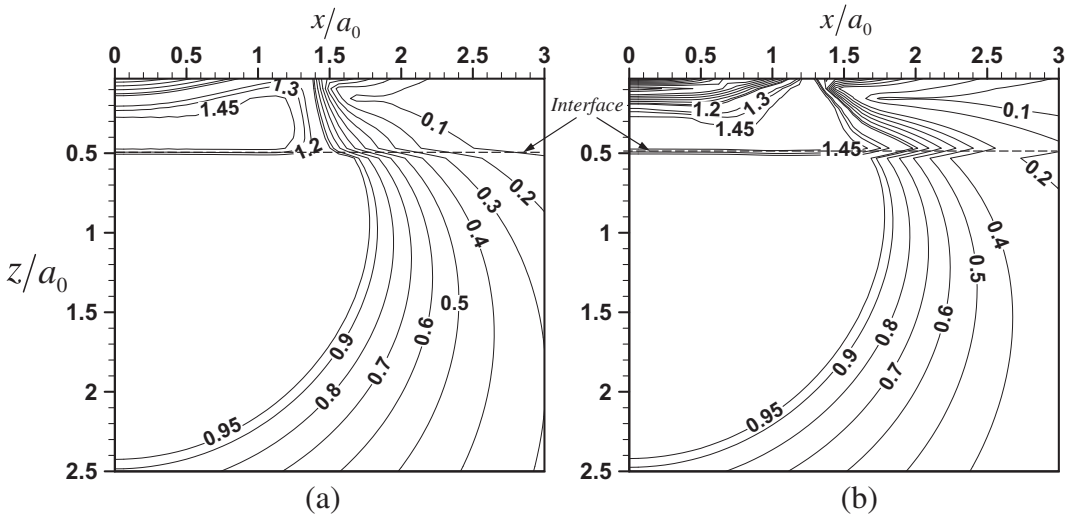

Fig. 10. Contours of von Mises stress σ_{VM}/σ_{Ys} in the cross section of $y = 0$ under the normal load of $W = 30W_c$: (a) the more compliant coating case ($E_c/E_s = 0.5$), and (b) the stiffer coating case ($E_c/E_s = 2$).

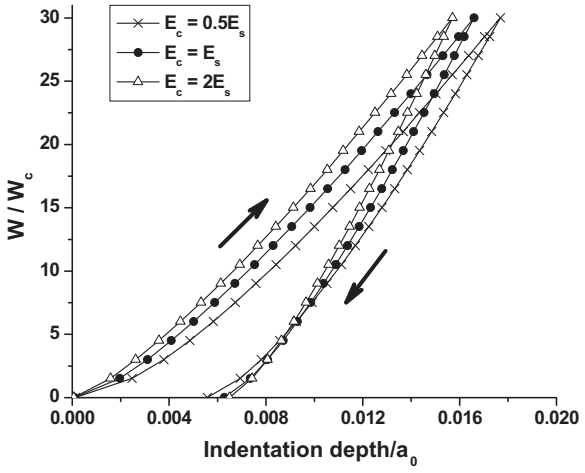

Fig. 11. Curves of indentation depth versus the applied normal load for cases with different modulus ratios.

are set to be equal, and the coating thickness is $t = 0.5a_0$. Fig. 12(a) shows the pressure profiles along the x-axis under the maximum load, which indicates that the increase in the yield strength of layer increases the contact pressure and reduces the real contact area (the dimensionless contact areas $A_c/\pi a_0^2$ are 2.095, 1.966, 1.841, 1.782, and 1.747 when the yield strength ratio σ_{Yc}/σ_{Ys} equals 0.75, 1, 1.5, 2, and 4, respectively). Fig. 12(b) gives the load–displacement curves. Because the moduli of layer are the same in these cases, the loading curves almost overlap under the light load, but deviate apart under heavy loads due to different plastic responses of the layer; the slopes of unloading curves are approximately the same. After unloading is completed, the residual impression is shallower in the case of a harder coating. The depth of the residual impression drops from $0.007a_0$ in the case of $\sigma_{Yc}/\sigma_{Ys} = 0.75$ to $0.0057a_0$ in the case of $\sigma_{Yc}/\sigma_{Ys} = 4$ (about 20% decrease). This part of the study has numerically reproduced the fact that increasing the layer yield strength enhances the hardness of the material system, which well matches the engineering practice of using a hard coating to increase the load bearing capacity.

The plastic regions in the cross section ($y = 0$) under the normal load of $W = 30W_c$ are presented in Fig. 12(c), where five types of lines represent the boundaries of plastic regions for the cases of $\sigma_{Yc}/\sigma_{Ys} = 0.75$, 1, 1.5, 2, and 4, respectively. For the case with the hardest coating ($\sigma_{Yc}/\sigma_{Ys} = 4$), plastic deformation only occurs in the substrate because the high material strength keeps the layer from yielding. This is consistent with the simulation results reported by Komvopoulos (1989). For the case of $\sigma_{Yc}/\sigma_{Ys} = 2$, a plastic region can be found in the layer beneath the contact surface, and the boundary of plastic region has significant discontinuity at the coating-substrate interface due to the large difference of material strengths. A harder coating can support the higher stress value, and therefore less material in the layer yields to resist the external load, which suggests that increasing σ_{Yc} improves the strength of a layered body. Using a softer coating may obviously expand the plastic region in the layer. For the case of $\sigma_{Yc}/\sigma_{Ys} = 1.5$, the plastic region reaches the surface, and an elastic core surrounded by the plastic region can be found just beneath the contact indenter. A continuous boundary of the plastic region is detected in the case of $\sigma_{Yc}/\sigma_{Ys} = 1.0$ (a homogeneous body). Further decreasing the layer yield strength ($\sigma_{Yc}/\sigma_{Ys} = 0.75$) removes the central elastic core and introduces a fully plastic state in the layer. It increases the possibility of wear caused by plastic deformation. In addition, increasing the layer yield strength slightly expands the plastic region in the substrate.

Radial cracking and layer buckling may be associated with the lateral stress developed in the layer perpendicular to the coating-substrate interface. The normal stress profiles σ_{11} along the depth at the origin when $W = 30W_c$ are presented in Fig. 12(d) for various layer yield strengths. The normal stresses σ_{11} near the contacting surface are found to be compressive, and the absolute magnitude of σ_{11} increases with the layer yield strength. In the layer, σ_{11} approximately keeps the constant value within the plastic region (larger in a harder coating), and varies linearly with the depth in the elastically deformed region. For the case of $\sigma_{Yc}/\sigma_{Ys} = 4$, σ_{11} becomes tensile at the interface, which may facilitate the propagation of cracks in the layer and orthogonal to the interface. In addition, the yield strength of the layer has negligible effect on the stress profiles of σ_{11} in the substrate.

4.4. Parametric study: thickness of the layer

The effects of the layer thickness on the contact performances are also investigated, and the simulation results from the cases of

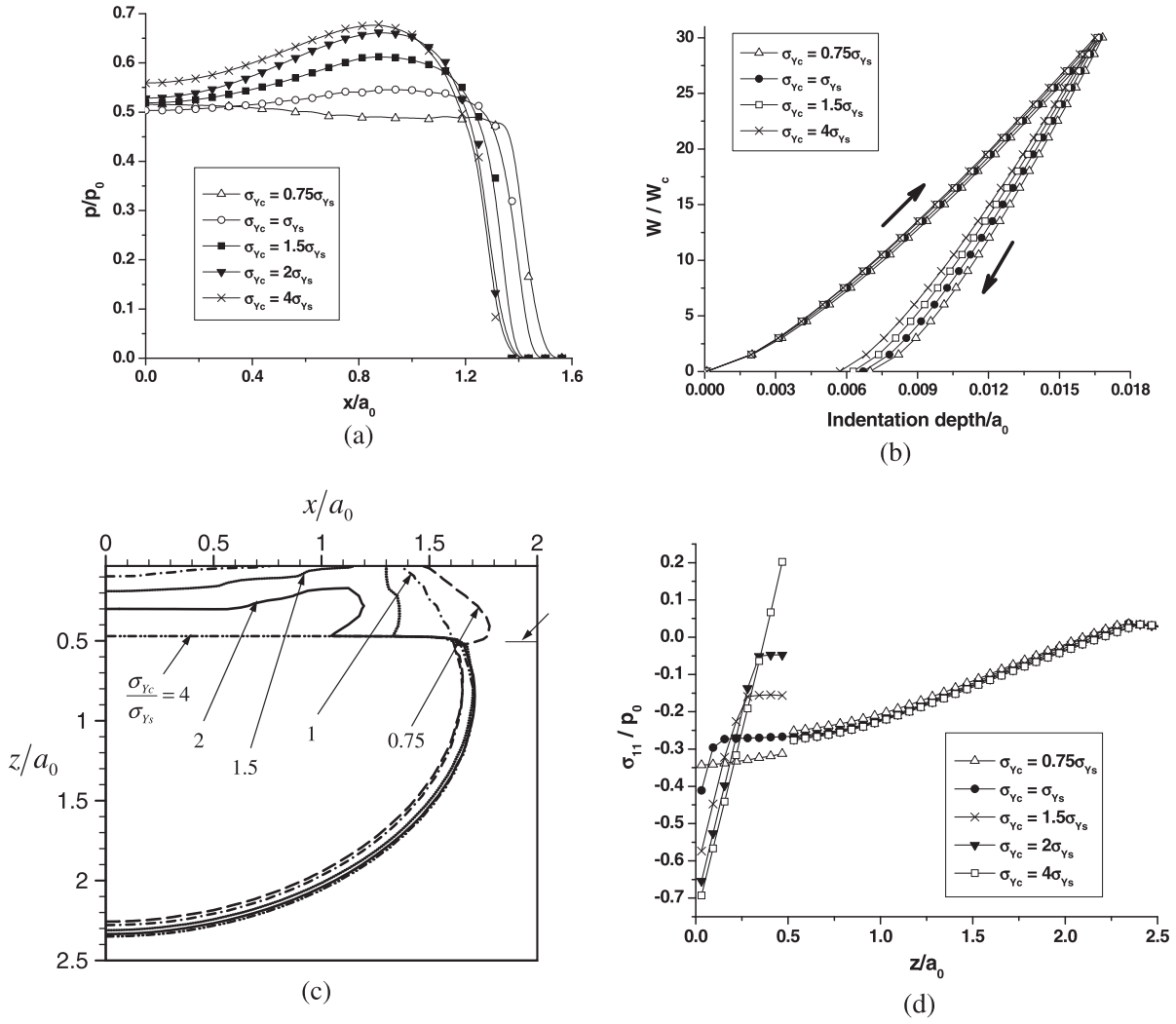

Fig. 12. Comparisons of cases with different yield strength ratios σ_{Yc}/σ_{Ys} ($E_c/E_s = 1$, $t/a_0 = 0.5$): (a) contact pressure along the x-axis when $W = 30W_c$, (b) indentation depth versus the applied load, (c) plastic regions in the plane of $y = 0$ when $W = 30W_c$ (the dashed, dot-dashed, dotted, solid, and dot-dot-dashed lines are the boundaries of plastic regions for cases of $\sigma_{Yc}/\sigma_{Ys} = 0.75$, 1, 1.5, 2, and 4, respectively), and (d) normal stress σ_{11} along the depth at the origin when $W = 30W_c$.

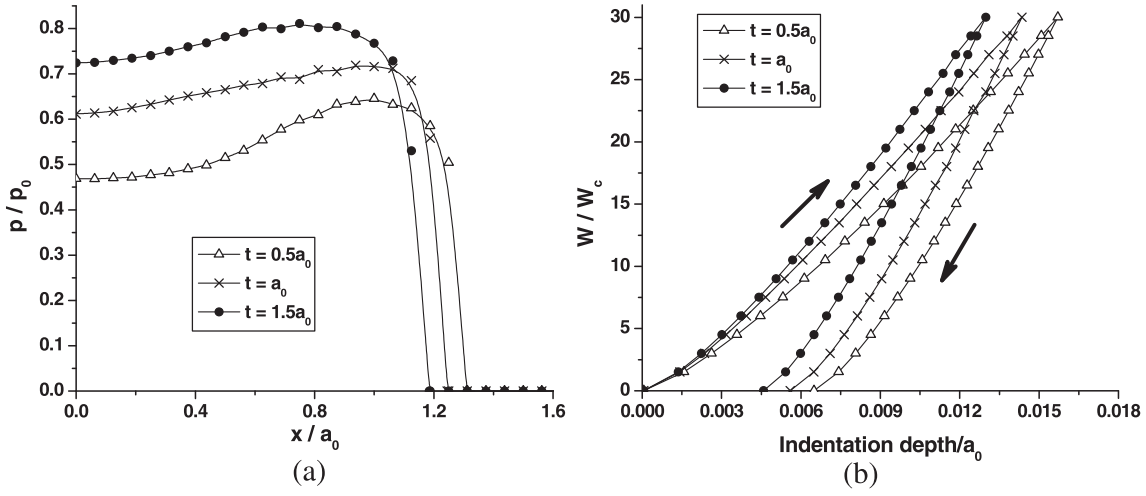

Fig. 13. Comparisons of cases with different coating thicknesses t ($\sigma_{Yc}/\sigma_{Ys} = 1.5$, $E_c/E_s = 2$): (a) contact pressure along the x-axis when $W = 30W_c$, and (b) indentation depth versus the applied load.

$t/a_0 = 0.5$, 1, 1.5 are presented and compared in Fig. 13. In these cases, the Young's modulus ratio and the yield strength ratio are fixed to be $E_c/E_s = 2$ and $\sigma_{Yc}/\sigma_{Ys} = 1.5$ (the harder and stiffer coating), respectively. Fig. 13(a) gives the pressure distributions along the x-axis under the maximum indentation load. The increase in the coating thickness increases the pressure and shrinks the

contact area (the dimensionless contact areas $A_c/\pi a_0^2$ are 1.682, 1.493, and 1.349 when the dimensionless coating thickness t/a_0 equals 0.5, 1, and 1.5, respectively). The load–displacement curves are presented in Fig. 13(b), where increasing the layer thickness increases the slopes of loading and unloading curves (higher stiffness) and yields a shallower residual impression (higher strength).

Fig. 13 reveals that increasing the layer thickness may be an effective approach to achieving the high hardness and high stiffness for a body with a harder and stiffer coating. However, in real engineering practices, coating thickness is also limited by cost considerations.

5. Conclusions

A fast semi-analytical three-dimensional model is developed for the elasto-plastic contact of layered materials, and used to analyze the contact behaviors of a rigid ball over a layered elasto-plastic half-space. This model treats the topmost layer as an inhomogeneous inclusion and introduces equivalent eigenstrains into the layer to account for the stress disturbance due to material dissimilarity of the layer and the substrate.

Excellent agreements are found between the numerical results from the present model and those from an analytical solution, from an experimental measurement, and from the finite element simulation. These comparisons validate the propriety and accuracy of this model. A group of contact simulations is performed with various layer parameters: elastic moduli, yield strengths, and thicknesses. Numerical analyses indicate that a harder coating can reinforce the strength of a layered body and shrink the plastic region in layer; however, a coating with too high strength may accompany a tensile lateral stress at the interface, which may lead to crack propagation there. A stiffer coating enhances the stiffness of the body while enlarging the plastic region in the layer. With a harder or a stiffer coating, the peak pressure occurs near the contact edge under a relatively heavy load $W = 30W_c$. For the purpose of improving the load bearing capacity and reducing the potential of plasticity wear, the layer with a higher hardness and a lower Young's modulus should be chosen.

Acknowledgements

Research supports from US Office of Naval Research, Department of Energy, and the Timken Company are sincerely acknowledged by the authors.

Appendix A

A.1. Stress solutions of a unit normal force at the surface origin of a half-space (T_{ij}^n)

$$T_{11}^n(x,y,z) = \frac{1}{2\pi}\left[\frac{1-2\nu_s}{r^2}\left\{\left(1-\frac{z}{\rho}\right)\frac{x^2-y^2}{r^2}+\frac{zy^2}{\rho^3}\right\}-\frac{3zx^2}{\rho^5}\right]$$

$$T_{22}^n(x,y,z) = T_{11}^n(y,x,z)$$

$$T_{33}^n(x,y,z) = -\frac{3}{2\pi}\frac{z^3}{\rho^5}$$

$$T_{12}^n(x,y,z) = \frac{1}{2\pi}\left[\frac{1-2\nu_s}{r^2}\left\{\left(1-\frac{z}{\rho}\right)\frac{xy}{r^2}-\frac{xyz}{\rho^3}\right\}-\frac{3xyz}{\rho^5}\right]$$

$$T_{13}^n(x,y,z) = -\frac{3}{2\pi}\frac{xz^2}{\rho^5}$$

$$T_{23}^n(x,y,z) = T_{13}^n(y,x,z)$$

A.2. Stress solutions of a unit tangential force at the surface origin of a half-space (T_{ij}^t)

$$T_{11}^t(x,y,z) = \frac{1}{2\pi}\left[-\frac{3x^3}{\rho^5}+(1-2\nu_s)\times\left\{\frac{x}{\rho^3}-\frac{3x}{\rho(\rho+z)^2}+\frac{x^3}{\rho^3(\rho+z)^2}+\frac{2x^3}{\rho^2(\rho+z)^3}\right\}\right]$$

$$T_{22}^t(x,y,z) = \frac{1}{2\pi}\left[-\frac{3xy^2}{\rho^5}+(1-2\nu_s)\times\left\{\frac{x}{\rho^3}-\frac{x}{\rho(\rho+z)^2}+\frac{xy^2}{\rho^3(\rho+z)^2}+\frac{2xy^2}{\rho^2(\rho+z)^3}\right\}\right]$$

$$T_{33}^t(x,y,z) = -\frac{3}{2\pi}\frac{xz^2}{\rho^5}$$

$$T_{12}^t(x,y,z) = \frac{1}{2\pi}\left[-\frac{3x^2y}{\rho^5}+(1-2\nu_s)\times\left\{-\frac{y}{\rho(\rho+z)^2}+\frac{x^2y}{\rho^3(\rho+z)^2}+\frac{2x^2y}{\rho^2(\rho+z)^3}\right\}\right]$$

$$T_{13}^t(x,y,z) = -\frac{3}{2\pi}\frac{x^2z}{\rho^5}$$

$$T_{23}^t(x,y,z) = -\frac{3}{2\pi}\frac{xyz}{\rho^5}$$

*A.3. Indefinite double integrals of T_{ij}^n about **x** and **y***

$$\iint T_{11}^n(x,y,z)\,dx\,dy = \frac{1}{2\pi}\left[-2\nu_s\theta_\rho+2(1-2\nu_s)\tan^{-1}\times\left(\frac{x}{\rho+y+z}\right)-\frac{xz}{\rho(\rho+y)}\right]$$

$$\iint T_{22}^n(x,y,z)\,dx\,dy = \frac{1}{2\pi}\left[-2\nu_s\theta_\rho+2(1-2\nu_s)\tan^{-1}\times\left(\frac{y}{\rho+x+z}\right)-\frac{yz}{\rho(\rho+x)}\right]$$

$$\iint T_{33}^n(x,y,z)\,dx\,dy = \frac{1}{2\pi}\left[-\theta_\rho+\frac{xz}{\rho(\rho+y)}+\frac{yz}{\rho(\rho+x)}\right]$$

$$\iint T_{12}^n(x,y,z)\,dx\,dy = \frac{1}{2\pi}\left[(2\nu_s-1)\ln(\rho+z)-\frac{z}{\rho}\right]$$

$$\iint T_{13}^n(x,y,z)\,dx\,dy = \frac{1}{2\pi}\left[-\frac{z^2}{\rho(\rho+y)}\right]$$

$$\iint T_{23}^n(x,y,z)\,dx\,dy = \frac{1}{2\pi}\left[-\frac{z^2}{\rho(\rho+x)}\right]$$

*A.4. Indefinite double integrals of T_{ij}^t about **x** and **y***

$$\iint T_{11}^t(x,y,z)\,dx\,dy = \frac{1}{2\pi}\left[2\gamma_y+z(1-2\nu_s)\left(\frac{y}{\rho(\rho+z)}+\frac{z}{\rho(\rho+y)}\right)-\frac{2\nu_s x^2}{\rho(\rho+y)}\right]$$

$$\iint T_{22}^t(x,y,z)\,dx\,dy = \frac{1}{2\pi}\left[2\nu_s\gamma_y-z(1-2\nu_s)\frac{y}{\rho(\rho+z)}-\frac{2\nu_s y}{\rho}\right]$$

$$\iint T_{33}^t(x,y,z)\,dx\,dy = \frac{1}{2\pi}\left[-z^2/\rho(\rho+y)\right]$$

$$\iint T_{12}^t(x,y,z)\,dx\,dy = \frac{1}{2\pi}\left[\gamma_x-z(1-2\nu_s)\frac{x}{\rho(\rho+z)}-\frac{2\nu_s x}{\rho}\right]$$

$$\iint T^t_{13}(x,y,z)dxdy = \frac{1}{2\pi}\left[-\frac{xz}{\rho(\rho+y)} - \tan^{-1}\left(\frac{xy}{z\rho}\right)\right]$$

$$\iint T^t_{23}(x,y,z)dxdy = \frac{1}{2\pi}(-z/\rho)$$

A.5. Indefinite triple integrals of T^n_{ij} about ***x,y***, and ***z***

$$\iiint T^n_{11}(x,y,z)dxdydz = \frac{1}{2\pi}\left[2v_s y\gamma_x - 2(1-v_s)z\theta_x - 2v_s z\theta_y + \frac{4z(1-v_s)v_s}{1-2v_s}\theta_z + \frac{zv_s}{1-2v_s}\theta_\rho\right]$$

$$\iiint T^n_{22}(x,y,z)dxdydz = \frac{1}{2\pi}\left[2v_s x\gamma_y - 2(1-v_s)z\theta_y - 2v_s z\theta_x + \frac{4z(1-v_s)v_s}{1-2v_s}\theta_z + \frac{zv_s}{1-2v_s}\theta_\rho\right]$$

$$\iiint T^n_{33}(x,y,z)dxdydz = \frac{1}{2\pi}\left[2(x\gamma_y + y\gamma_x) - 2v_s z(\theta_x+\theta_y) + \frac{4z(1-v_s)^2}{1-2v_s}\theta_z + \frac{z(1-v_s)}{1-2v_s}\theta_\rho\right]$$

$$\iiint T^n_{12}(x,y,z)dxdydz = \frac{1}{2\pi}[-2v_s\rho - (1-2v_s)z\gamma_z]$$

$$\iiint T^n_{13}(x,y,z)dxdydz = \frac{1}{2\pi}[2x\theta_x + y\gamma_z]$$

$$\iiint T^n_{23}(x,y,z)dxdydz = \frac{1}{2\pi}[2y\theta_y + x\gamma_z]$$

where

$$r^2 = x^2+y^2, \quad \rho = \sqrt{x^2+y^2+z^2}$$

$$\theta_x = \tan^{-1}\left(\frac{\rho+y+z}{x}\right), \quad \theta_y = \tan^{-1}\left(\frac{\rho+x+z}{y}\right),$$

$$\theta_z = \tan^{-1}\left(\frac{\rho+x+y}{z}\right)$$

$$\theta_\rho = \tan^{-1}\left(\frac{xy}{z\rho}\right), \quad \gamma_x = \ln(x+\rho),$$

$$\gamma_y = \ln(y+\rho), \quad \gamma_z = \ln(z+\rho)$$

References

Antaluca, E., Nelias, D., 2008. Contact fatigue analysis of a dented surface in a dry elastic–plastic circular point contact. Tribol. Lett. 29 (2), 139–153.

Bhushan, B., Peng, W., 2002. Contact mechanics of multilayered rough surfaces. ASME Appl. Mech. Rev. 55, 435–479.

Bolshakov, A., Oliver, W.C., Pharr, G.M., 1996. On the measurement of mechanical properties using nanoindentation: Part II. Finite element simulations. J. Mater. Res. 11, 760–768.

Boucly, V., Nelias, D., Liu, S.B., Wang, Q., Keer, L.M., 2005. Contact analyses for bodies with frictional heating and plastic behavior. ASME J. Tribol. 127, 355–364.

Boucly, V., Nelias, D., Green, I., 2007. Modeling of the rolling and sliding contact between two asperities. ASME J. Tribol. 129, 235–245.

Burmister, D.M., 1945. The general theory of stresses and displacements in layered systems. J. Appl. Phys. 16, 89–94.

Carlsson, S., Larsson, P.-L., 2001. On the determination of residual stress and strain fields by sharp indentation testing. Part I: theoretical and numerical analysis. Acta Mater. 49, 2179–2191.

Chen, W.T., 1971. Computation of stresses and displacements in a layered elastic medium. Int. J. Eng. Sci. 9, 775–799.

Chen, W.W., Wang, Q., Liu, Y.C., Chen, W., Cao, J., Xia, C., Talwar, R., Lederich, R., 2007. Analysis and convenient formulas for elasto-plastic contacts of nominally flat surfaces: average gap, contact area ratio, and plastically deformed volume. Tribol. Lett. 28, 27–38.

Chen, W.W., Wang, Q., 2008. Thermomechanical analysis of elasto-plastic bodies in a sliding spherical contact and the effects of sliding speed, heat partition, and thermal softening. ASME J. Tribol. 130, 041402.

Chen, W.W., Liu, S.B., Wang, Q.J., 2008a. Fast Fourier transform based numerical methods for elasto-plastic contacts of nominally flat surfaces. ASME J. Appl. Mech. 75, 011022.

Chen, W.W., Wang, Q., Wang, F., Keer, L.M., Cao, J., 2008b. Three-dimensional repeated elasto-plastic point contacts, rolling, and sliding. ASME J. Appl. Mech. 75, 021021.

Chiu, Y.P., 1978. On the stress field and surface deformation in a half space with a cuboidal zone in which initial strains are uniform. ASME J. Appl. Mech. 45, 302–306.

Chiu, Y.P., 1980. On the internal stresses in a half-plane and a layered containing localized inelastic strains or inclusions. ASME J. Appl. Mech. 47, 313–318.

Cho, S.-J., Lee, K.-R., Eun, K.Y., Hahn, J.H., Ko, D.-H., 1999. Determination of elastic modulus and Poisson's ratio of diamond-like carbon films. Thin Solid Films 341, 207–210.

Follansbeea, P.S., Sinclairb, G.B., 1984. Quasi-static normal indentation of an elasto-plastic half-space by a rigid sphere—I: Analysis. Int. J. Solids Struct. 20, 81–91.

Giannakopoulos, A.E., 2003. The influence of initial elastic surface stresses on instrumented sharp indentation. ASME J. Appl. Mech. 70, 638–643.

Hardy, C., Baronet, C.N., Tordion, G.V., 1971. The elasto-plastic indentation of a half-space by a rigid sphere. Int. J. Numer. Methods Eng. 3, 451–462.

Jacq, C., Nelias, D., Lormand, G., Girodin, D., 2002. Development of a three-dimensional semi-analytical elastic–plastic contact code. ASME J. Tribol. 124, 653–667.

Johnson, K.L., 1985. Contact Mechanics. Cambridge University Press, London.

Ju, F.D., Chen, T.Y., 1984. Thermomechanical cracking in layered media from moving friction load. ASME J. Tribol. 106, 513–518.

Kennedy, F.E., Ling, F.F., 1974. Elasto-plastic indentation of a layered medium. ASME J. Eng. Mater. Technol. 96, 97–103.

Komvopoulos, K., 1989. Elastic–plastic finite element analysis of indented layered media. ASME J. Tribol. 111, 430–439.

Kral, E.R., Komvopoulos, K., 1996. Three-dimensional finite element analysis of surface deformation and stresses in an elastic–plastic layered medium subjected to indentation and sliding contact loading. ASME J. Appl. Mech. 63, 365–375.

Kral, E.R., Komvopoulos, K., 1997. Three-dimensional finite element analysis of subsurface stress and strain fields due to sliding contact on an elastic–plastic layered medium. ASME J. Tribol. 119, 332–341.

Liu, S.B., Wang, Q., 2002. Studying contact stress fields caused by surface tractions with a discrete convolution and fast Fourier transform algorithm. ASME J. Tribol. 124, 36–45.

Liu, S.B., Peyronnel, A., Wang, Q.J., Keer, L.M., 2005. An extension of the Hertz theory for three-dimensional coated bodies. Tribol. Lett. 18, 303–314.

Liu, S.B., Wang, Q., Liu, G., 2000. A versatile method of discrete convolution and FFT (DC-FFT) for contact analyses. Wear 243, 101–111.

Liu, Y.C., Chen, W.W., Zhu, D., Liu, S.B., Wang, Q.J., 2007. An elastohydrodynamic lubrication model for coated surfaces in point contacts. ASME J. Tribol. 129, 509–516.

Love, A.E.H., 1929. The stress produced in a semi-infinite solid by pressure on part of the boundary. Philos. Trans. Royal Soc. London A228, 377–420.

Mesarovic, S.D., Fleck, N.A., 1999. Spherical indentation of elastic–plastic solids. Proc. Royal Soc. London A 455, 2707–2728.

Michler, J., Tobler, M., Blank, E., 1999. Thermal annealing behavior of alloyed DLC films on steel: determination and modeling of mechanical properties. Diam. Relat. Mater. 8, 510–516.

Mura, T., 1982. Micromechanics of Defects in Solids. Martinus Nijhoff, The Hague.

Nelias, D., Antaluca, E., Boucly, V., 2007a. Rolling of an elastic ellipsoid upon an elastic–plastic flat. ASME J. Tribol. 129, 791–800.

Nelias, D., Antaluca, E., Boucly, V., Cretu, S., 2007b. A three-dimensional semianalytical model for elastic–plastic sliding contacts. ASME J. Tribol. 129, 761–771.

Nelias, D., Boucly, V., Brunet, M., 2006. Elastic–plastic contact between rough surfaces: proposal for a wear or running-in model. ASME J. Tribol. 128, 236–244.

Nogi, T., Kato, T., 1997. Influence of a hard surface layer on the limit of elastic contact –Part I: Analysis using a real surface model. ASME J. Tribol. 119, 493–500.

O'Sullivan, T.C., King, R.B., 1988. Sliding contact stress field due to a spherical indenter on a layered elastic half-space. ASME J. Tribol. 110, 235–240.

Peng, W., Bhushan, B., 2001. A numerical three-dimensional model for the contact of layered elastic/plastic solids with rough surfaces by a variational principle. ASME J. Tribol. 123, 330–342.

Peng, W., Bhushan, B., 2002. Sliding contact analysis of layered elastic/plastic solids with rough surfaces. ASME J. Tribol. 124, 46–61.

Plumet, S., Dubourg, M.-C., 1998. A 3-D model for a multilayered body loaded normally and tangentially against A rigid body: application to specific coatings. ASME J. Tribol. 120, 668–676.

Polonsky, I.A., Keer, L.M., 1999. A numerical method for solving rough contact problems based on multi-level multi-summation and conjugate gradient techniques. Wear 231, 206–219.

Polonsky, I.A., Keer, L.M., 2000. A fast and accurate method for numerical analysis of elastic layered contacts. ASME J. Tribol. 122, 30–35.

Polonsky, I.A., Keer, L.M., 2001. Stress analysis of layered elastic solids with cracks using the fast Fourier transform and conjugate gradient techniques. ASME J. Appl. Mech. 68, 708–714.

Suresh, S., Giannakopoulos, A.E., 1998. A new method for estimating residual stresses by instrumented sharp indentation. Acta Mater. 46, 5755–5767.

Tian, H., Saka, N., 1991. Finite element analysis of an elastic–plastic two-layer half-space: sliding contact. Wear 148, 261–285.

Tichy, J.A., Meyer, D.M., 2000. Review of solid mechanics in tribology. Int. J. Solids Struct. 37, 391–400.

Wang, F., Keer, L.M., 2005. Numerical simulation for three dimensional elastic–plastic contact with hardening behavior. ASME J. Tribol. 127, 494–502.

Ye, N., Komvopoulos, K., 2003. Effect of residual stress in surface layer on contact deformation of elastic–plastic layered media. ASME J. Tribol. 125, 692–699.

Zhou, K., Chen, W.W., Keer, L.M., Wang, Q.J., 2009. A fast method for solving three-dimensional arbitrarily-shaped inclusions in a half-space. Comput. Methods Appl. Mech. Eng. 198, 885–892.

Zhou, K., Keer, L.M., Wang, Q.J., Ai, X., Sawamiphakdi, K., Glaws, P., Paire, M., under review. Interactions of multiple arbitrarily-shaped 3D inhomogeneous inclusions in a half space: method and novel application to film-substrate systems.